Investigation of crack patterns and cyclic performance of Ti–Si nanocomposite thin film anodes for lithium ion batteries

Y.H. Wang[a], Y. He[a], R.J. Xiao[a], H. Li[a,*], K.E. Aifantis[b], X.J. Huang[a]

[a] Beijing National Laboratory for Condensed Matter Physics, Institute of Physics, Chinese Academy of Sciences, Beijing 100190, China
[b] Lab of Mechanics and Materials, Aristotle University of Thessaloniki, Thessaloniki 54124, Greece

ARTICLE INFO

ABSTRACT

Three different Ti–Si nanocomposite thin films are prepared by the co-sputtering method with Si target and Ti target. The film thickness ranges between 250 and 480 nm. X-ray diffraction (XRD), high resolution transmission electron miscopy (HRTEM) and X-ray photoelectron spectroscopy (XPS) reveal significant charge transfer between Ti and Si and uniform dispersion of Ti–Si alloy nanograins in the amorphous Si thin films. It is found that decreasing the grain size of the Ti_xSi_y alloy below 2 nm, can improve the cyclic performance over pure Si thin film electrodes and those containing larger Ti–Si grains. This is mainly related to the improved mechanical properties that result from dispersing small grains of Ti–Si. The throughout thin film cracks formed after 10 electrochemical cycles are finer and more curved compared to the other thin films with the same film thickness. Furthermore, the width of the cracks, as well as, the area and junction angles of the remained fractured particle size of all electrode films considered, is compared and analyzed, after 10 cycles.

© 2011 Elsevier B.V. All rights reserved.

1. Introduction

Silicon is a promising anode material for lithium ion batteries due to its large gravimetric and volumetric capacity. Electrochemical alloying reaction of lithium with silicon has been widely studied since the 1970s [1–3]. It has been well known that main difficulties for using silicon-based materials are caused by their dramatic 320% volume expansion and subsequent contraction during Li insertion and extraction ($19.6\,\text{Å}^3$ of Si to $82.5\,\text{Å}^3$ for $Li_{22}Si_5$). This leads to the pulverization of the electrode materials and poor cyclic performance [3]. As a result, the initially high capacity obtained (theoretical capacity of $Li_{4.4}Si$ is $4200\,\text{mAh}\,\text{g}^{-1}$) from several micrometer sized Si powder electrodes drops below $500\,\text{mAh}\,\text{g}^{-1}$ during initial cycling [4]. In 1999, the lithium storage behavior of silicon nanoparticles (SiNPs) and Si nanowires was reported by us [4–6]. It was found that SiNPs showed a significant advantage in capacity retention compared to large particle sizes. However, SiNPs suffered serious electrochemical agglomeration [5]. In order to solve the volume variation problem, many efforts have been made, including embedding nanosized alloy particles in a carbon matrix [7–11] or shell [12,13], SiO_x anode [14], forming intermetallic compounds or composites, such as Fe–Si [15], Co–Si [16], and Cu–Si [17] alloy powder. It is suggested that inactive

transitional metal could improve the electronic contact and buffer the volume variation of active silicon phase. However, the detailed information about the influence of transitional metal on the volume variation of active Si phase has not been reported.

Thin film electrodes have the advantage for fundamental research due to their well-defined structure and the ability to not use binder and conductive additive in testing them as anodes. Particularly, silicon thin film electrodes have attracted the most attention due to their superior cyclic performance and high initial coulombic efficiency [18–20]. Alloy type thin film electrodes, such as Co–Si, Ag–Si, Fe–Si and Zr–Si have been investigated [21–25]. It has been shown that annealing treatment for the alloy films, existence of inactive transitional metal and decreasing the film thickness can improve the cyclic performances. Up to now, however, the modification of transitional metal on the mechanical stability of Si films has not been clarified.

In this work, Ti–Si nanocomposite thin films with different Ti grain sizes have been prepared on Ti/quartz by co-sputtering and used as anodes for the first time. The cracking feature of the electrode films after 10 cycles has been investigated and correlated to the electrochemical cyclic performance.

2. Experimental

It was noticed by us that Ti films have a better adherence to quartz substrates when compared to Cu films. Therefore, a Ti thin film with a thickness of 320 nm was deposited on a polished quartz

* Corresponding author. Tel.: +86 10 82648067; fax: +86 10 82649046.
E-mail address: hli@aphy.iphy.ac.cn (H. Li).

Table 1
Thin film electrode preparation conditions and features.

Films	Thickness (nm)	Deposition time (min)	Ti/Si (atom)	Grain size (nm)	Sputtering power of Ti and Si (W)
a	480	60	1:8.78	5	40/150
b	250	30	1:8.79	2	40/150
c	250	30	1:8.89	1–2	20/150
d	250	30	0:1	0	0/150

substrate by DC magnetron sputtering as the current collector for the electrochemical tests. The pure Si and Ti–Si composite thin films were deposited on the Ti/quartz substrate by co-sputtering with pure silicon target (99.999% purity) and pure titanium target (99.5%). The Ti deposition was controlled by DC power and the Si deposition was controlled by r.f. power. The pressure of the sputtering chamber reached approximately 2×10^{-4} Pa and then was kept at 0.5 Pa under high purity argon (99.999%) during deposition. The r.f. power was kept at 150 W with different targets. The DC power was 20 W and 40 W respectively. The deposition time was alternated between 30 and 60 min. The size of both the silicon target and the titanium target was 50.8 mm in diameter and 5 mm in thickness. The target–substrate distance was fixed at 15 cm. The area of each thin film electrode was 1 cm^2. It was previously mentioned that both Si and Ti–Si films were prepared. The films prepared are named a–d as listed in Table.1. Scanning transmission microscopy energy dispersive X-ray (SEM-EDAX) was used to identify the ratio of Ti and Si, and the thickness was measured via the SEM cross-section images. Then the structure of the thin films was analyzed by a X' Pert Pro MPD X-ray diffractometer (XRD) (Philips, Holland) using Cu Kα1 radiation (λ = 1.5405 Å), a highly resolution transmission electron microscopy (HRTEM) (Tecnai G2 F20 U-TWIN) and a X-ray photoelectron spectrometer (XPS) (Escalab 250, Perkin Elmer Co.).

A Swagelok-type two-electrode cell was constructed using the thin film electrode as the working electrode and a lithium foil as the counter electrode. The electrolyte was 1 M LiPF$_6$ dissolved in ethylene carbonate (EC) and dimethyl carbonate (DMC) with a volume ratio of 1:1 (Shanghai Topsol Ltd., H$_2$O < 10 ppm). The cell was assembled in an argon-filled glove box and cycled between 5 mV and 3 V at room temperature using a Land automatic battery tester. After the 10th charge (delithiation), the electrodes were taken out from the cell and washed by anhydrous DMC in the argon-filled glove box and then dried in the vacuum chamber of the glove box before transferring to the vacuum chamber of the microscope for morphology investigation.

3. Results and discussions

3.1. Microstructure

The cross-section images of the thin film electrodes are shown in Fig. 1. The films are all dense and flat. The Ti–Si thin film a has a 480 nm thickness, while the other two Ti–Si thin films b and c, as well as the pure Si film d have the same thickness of 250 nm. The contact of the active layers with the substrate seems good for all films. In order to judge the homogeneity of the Ti–Si composite thin films, the Ti–Si composite thin films were also deposited on the Cu/quartz substrates under the same conditions for EDX mapping and XPS investigation. It can be seen in Fig. 2 that the distributions of Ti and Si are uniform in all three Ti–Si composite thin films.

The XRD patterns are shown in Fig. 3. It is seen that none of the films examined exhibited a crystalline Si pattern. Besides a broad diffraction pattern around 22° from quartz and the peak nearby 35° from Ti, only one peak around 38.2° and 37.2° can be observed
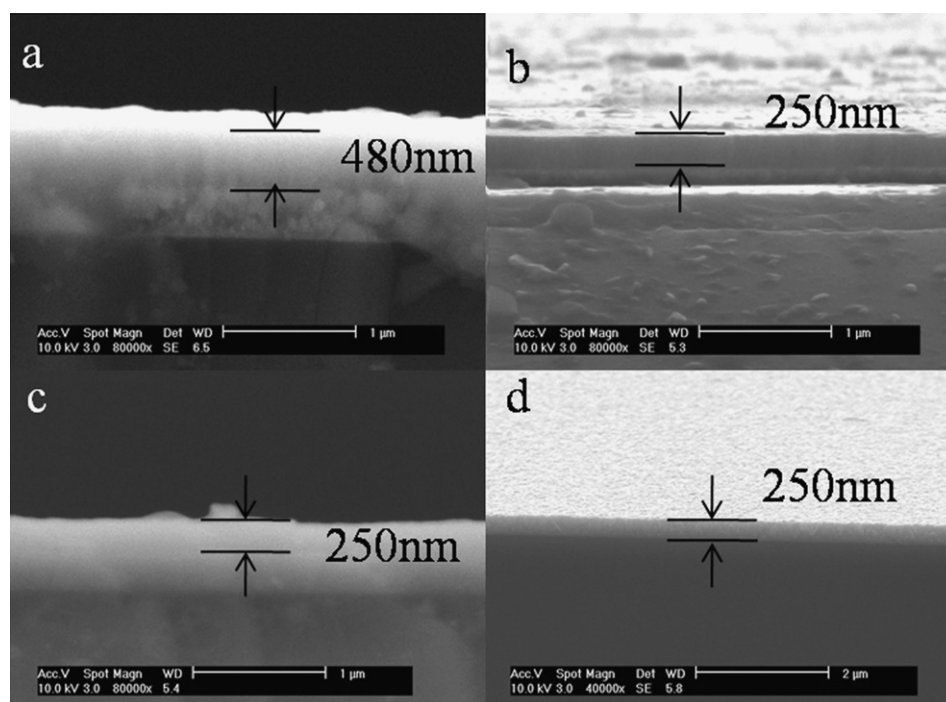

Fig. 1. SEM cross-section images of the thin film electrodes (a) Ti–Si nanocomposite thin film a; (b) Ti–Si nanocomposite thin film b; (c) Ti–Si nanocomposite thin film c; and (d) amorphous Si thin film d.
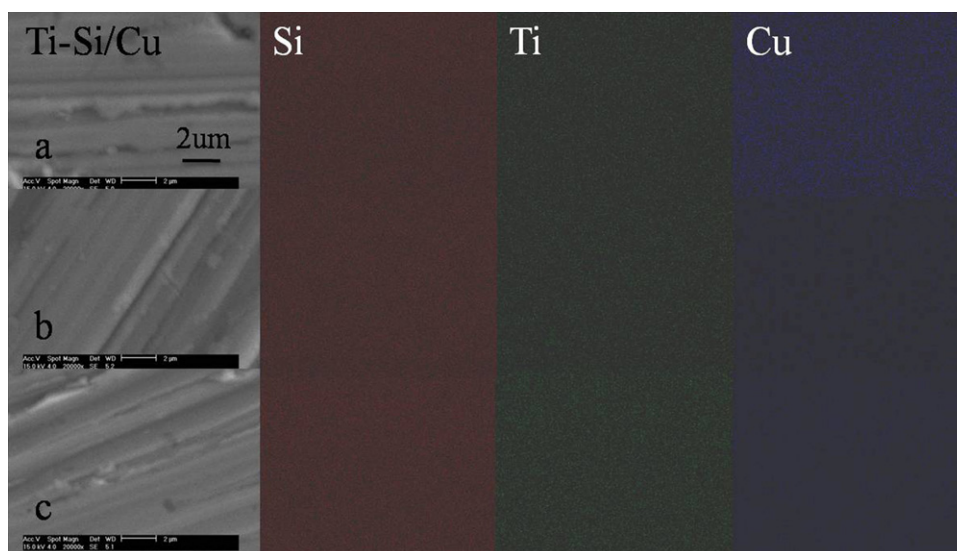
Fig. 2. SEM EDX element mapping images of all three Ti–Si alloy thin films *a*, *b* and *c*.

in the thin films *a* and *b*, which could be related to the diffraction patterns from Ti_xSi_y alloys (TiSi, Ti_5Si_3 or $TiSi_2$).

From the Raman spectra in Fig. 4, the band centered around 472 cm^{-1} (LO mode) can be observed clearly in all films, indicating a typical feature of amorphous silicon.

At a close inspection by TEM, some crystal grains about 5 nm large can be observed distinctly for the film *a* in Fig. 5a, which are dispersed in an amorphous matrix. The typical interplanar distances in the grains are 0.230 nm, 0.216 nm, 0.212 nm, 0.212 nm, and 0.208 nm respectively. The values are close to 0.224 nm for (1 0 1) plane of hexagonal Ti phase (JCPDS 44-1294), or 0.217 nm for the (1 1 2) plane of orthorhombic TiSi alloy phase (JCPDS 72-2115), or 0.220 nm for (2 1 1) plane of hexagonal Ti_5Si_3 phase (JCPDS 78-1429) or 0.209 nm for (0 2 2) plane for orthorhombic $TiSi_2$ phase (JCPDS 71-0187). It is not possible to assign it unambiguously to one phase due to poor crystallinity shown in the SAED pattern. For the film *b*, the stripes of the grain are not obvious, but the existence of small grains about 2 nm can be observed. In the film *c*, no crystalline grains can be observed but the contrast of the image shows a variation at 1–2 nm. It seems that Ti exists as amorphous domains. The size of the domains is about 1–2 nm. The film *d* is amorphous Si without showing contrast variation.

The XPS spectra shown in Fig. 6 were obtained after 3 min of Ar etching. The spectra have been corrected based on the binding energies of carbon. The binding energy of Si 2p 3/2 shifts towards lower energy in the two Ti–Si composite thin films *a* and *c* compared to the pure Si thin film as shown in Fig. 6A. It is not clear why the thin film *b* shows a positive shift, indicating a more oxidized state. Among the three Ti–Si thin films, the binding energies of Ti 2p 3/2 and Ti 2p1/2 for the thin film *c* shift more positive than that for the others. The observed shift of Si and Ti is consistent with reported results of $TiSi_2$ alloy [26,27]. The existence of Ti clusters could remove the band gap of amorphous Si and lead to a metallic band structure [28]. It should be mentioned that the appearance of shoulder peaks in Fig. 6 could indicate the trace amount of surface oxides and nitrides.

According to the above characterizations, Ti is distributed in the amorphous Si thin film uniformly for all films *a*, *b*, and *c*. The grain sizes vary from 1 nm to 5 nm. Small grains could be certain types of Ti–Si alloy. Obvious charge transfer between Ti and Si occurs.

3.2. Electrochemical performance

Fig. 7 compares the discharge and charge curves of the three Ti–Si composite thin films and Si thin film electrodes for the first
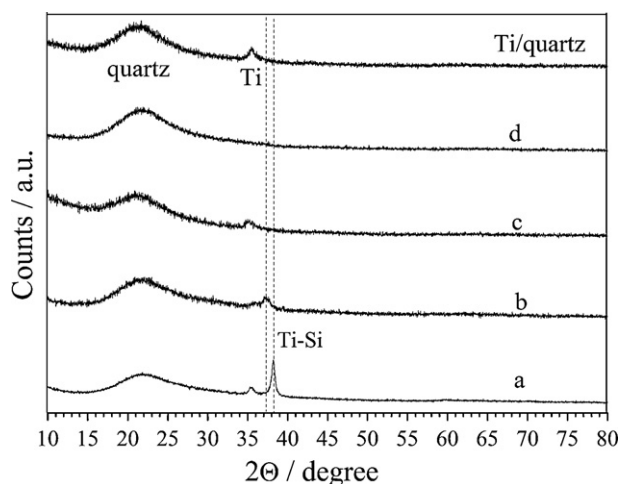

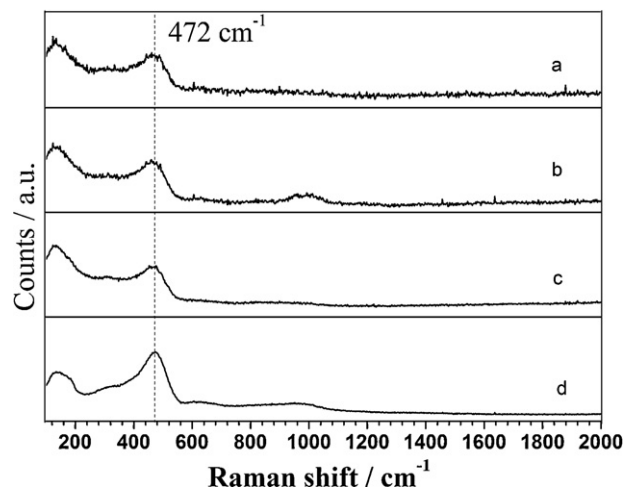**Fig. 3.** XRD patterns of Ti/quartz and the four thin film electrodes *a*–*d*.

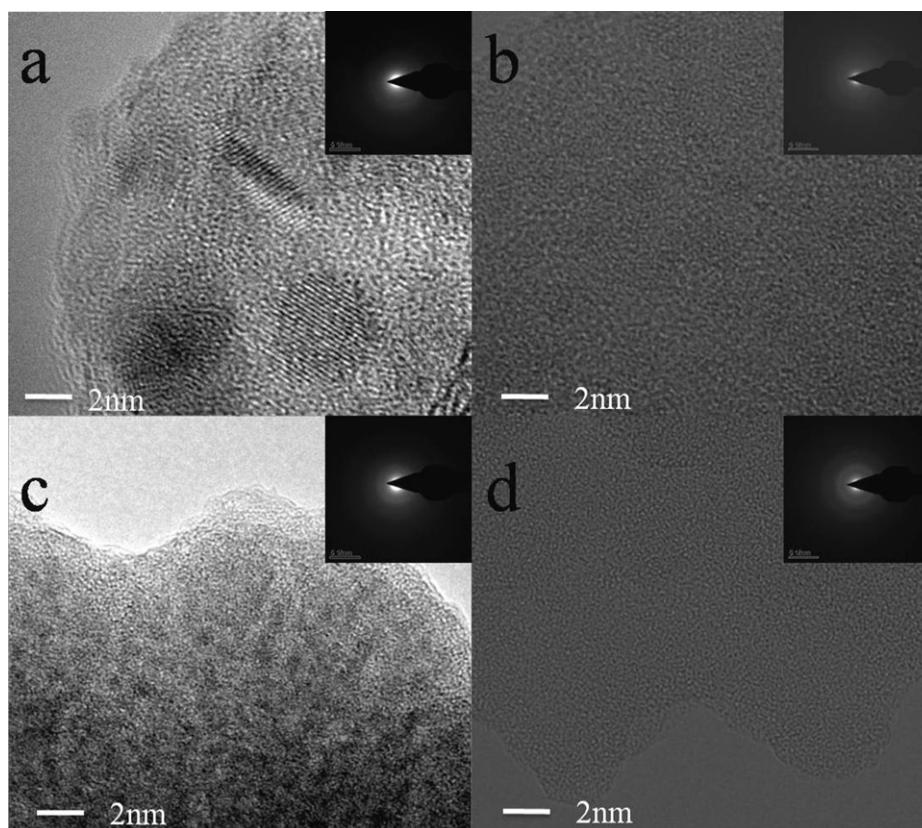**Fig. 4.** Raman spectra of the four thin film electrodes *a*–*d*.

Fig. 5. HRTEM images of the four thin film electrodes *a–d*.

20 cycles. The voltage profiles show a sloped feature and the lithium insertion voltage ranges mainly from 0.5 to 0 V at 0.1 C. These are typical features for room temperature Li–Si alloy reactions [4–6]. Compared to the amorphous pure silicon thin film, the Ti–Si nanocomposite thin films show higher initial coulombic efficiency and better cyclic performance, especially the film *c*. Furthermore,

the cyclic performance is also shown in Fig. 8. It can be seen that the thin film electrode *c* in which finer Ti_xSi_y alloy grains dispersed within amorphous Si thin film shows the best capacity retention.

According to the XPS results (Fig. 6), charge transfer occurs between Si and Ti in the Ti–Si nanocomposite thin films. It is of interest to understand whether the inclusion of Ti influences the
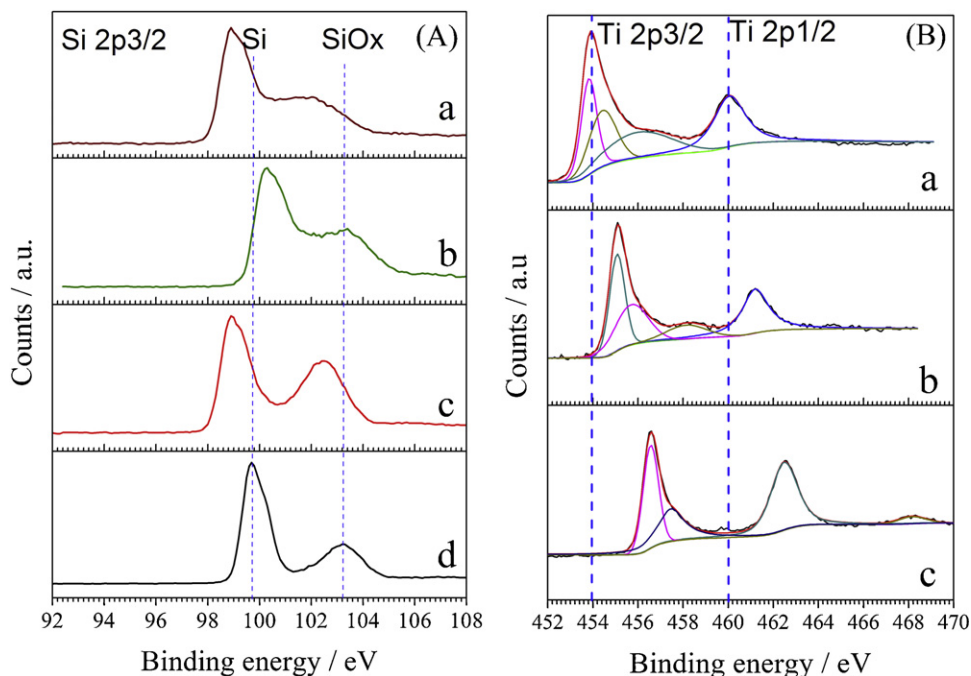

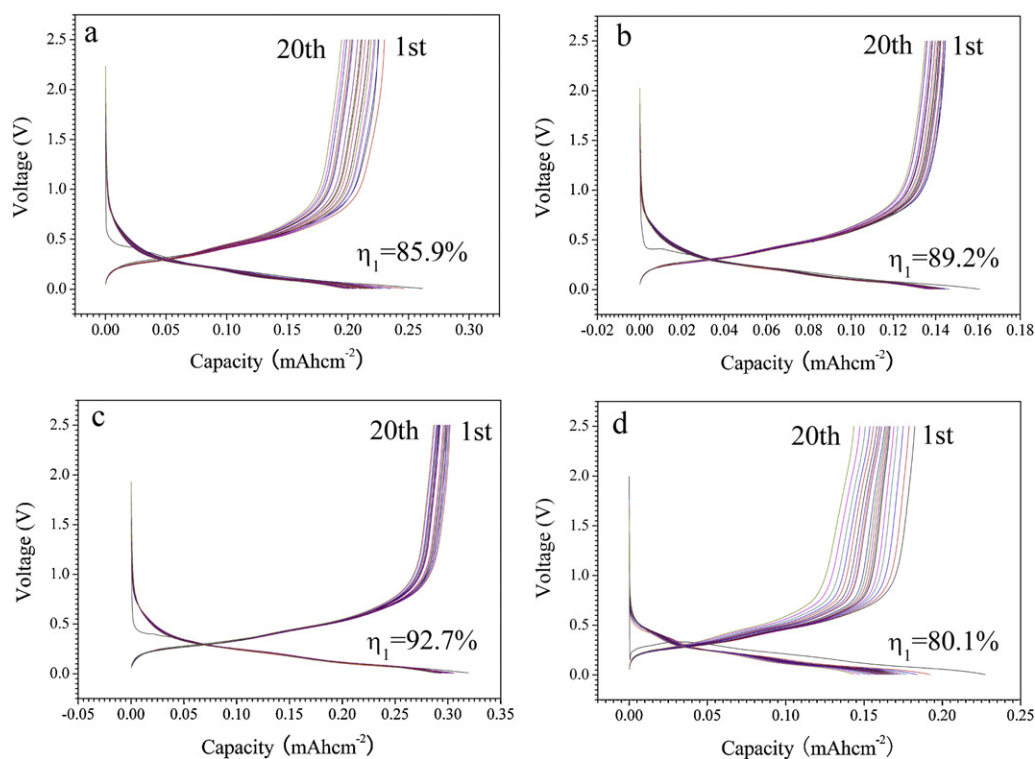**Fig. 6.** XPS spectra of the four thin film electrodes *a–d*: (A) Si 2p 3/2; (B) Ti 2p 3/2 and Ti 2p 1/2.

Fig. 7. The first 20 cycles of electrochemical profiles between 0.005 V and 2.5 V of the four thin film electrodes *a–d*.

Table 2
Voltage information of the four thin film electrodes deduced from the dQ/dV curves in Fig. 9.

Films	O1 (V)	O2 (V)	R1 (V)	R2 (V)	Δ(O1 − R1) (V)	Δ(O2 − R2) (V)	(O1 + R1)/2 (V)	(O2 + R2)/2 (V)
a	0.491	0.302	0.217	0.045	0.274	0.257	0.354	0.1735
b	0.450	0.279	0.217	0.065	0.233	0.214	0.3335	0.172
c	0.454	0.282	0.217	0.074	0.237	0.208	0.3355	0.178
d	0.479	0.282	0.217	0.049	0.262	0.233	0.348	0.1655

lithium insertion and extraction voltage significantly. Fig. 9 compares the dQ/dV curves of all electrodes at the second cycle. The electrode area, current density and other measuring conditions are the same for all thin films. The sum of the dQ/dV curves is listed in Table 2. The voltage of the first reduction peak (lithium insertion) R1 is 0.217 V for all electrodes. This means that the voltage of lithium insertion is not influenced significantly by the existence of Ti in the thin films in view of both thermodynamics and kinetics.

As listed in Table 2, no obvious variation and tendency about the polarization (Δ(O1 − R1), Δ(O2 − R2)) and average lithium insertion voltage ((O1 + R1)/2, (O2 + R2)/2) can be found. This means that the existence of Ti in the obtained nanostructures and composition and observed charge transfer of Ti to Si do not influence the kinetic and thermodynamic properties of the amorphous Si thin electrode significantly.

3.3. Fracture analysis

This presence of Ti, however, does affect the morphology/mechanical properties and hence the mechanical stability upon Li-insertion and de-insertion. Therefore the microstructure of these thin film electrodes after 10 electrochemical cycles is investigated. As shown in Figs. 10–13, the fracture responses differ between all the thin films examined even with the same thickness. It can be seen:

1) Films *a* and *d* show directional throughout film cracks while the films *b* and *c* show more branched and wiggle cracks. This is in agreement with theoretical studies [29] which predict that cracks are characterized by more branches and wiggles as the film thickness decreases. Furthermore, the observed crack patterns of the amorphous silicon film *d* are similar to those recently observed for 200–500 nm amorphous Si thin films on a stainless steel substrate after 10 cycles [29].
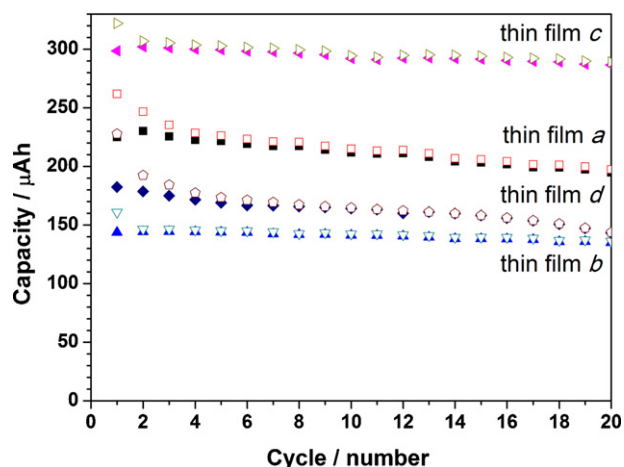

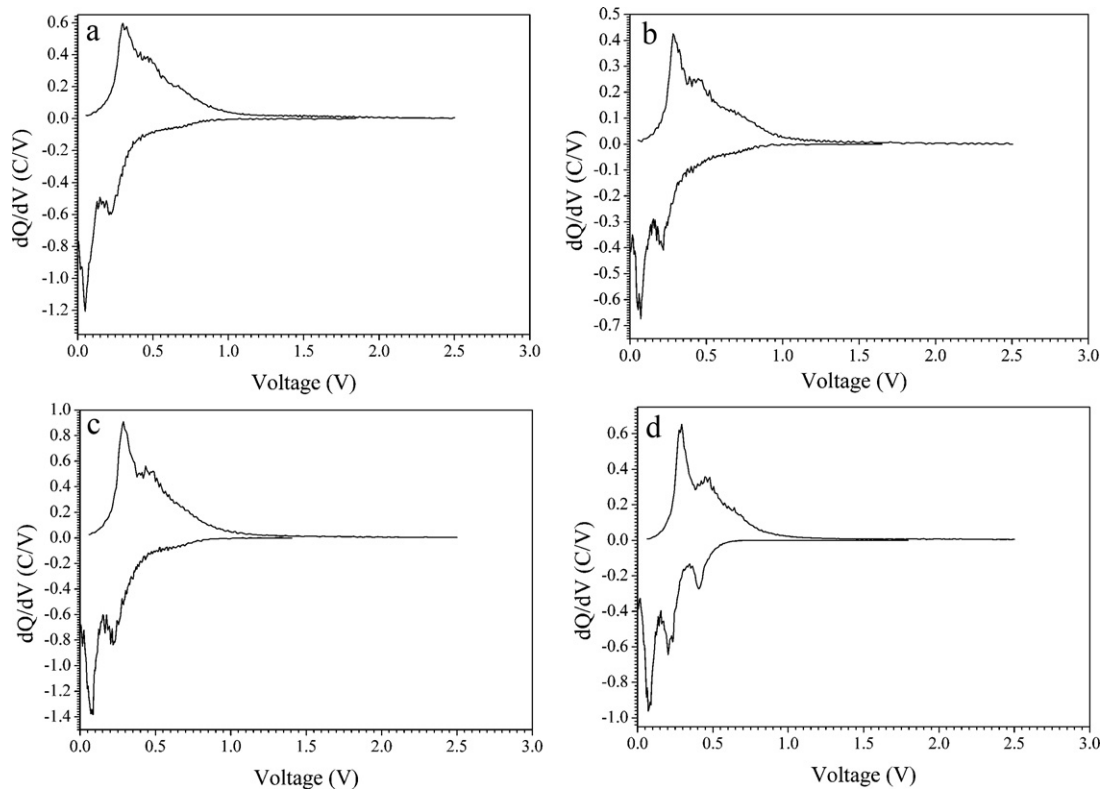**Fig. 8.** Cyclic performance of the four thin film electrodes *a–d*.

Fig. 9. dQ/dV curves of the four thin film electrodes *a–d* at the second cycle, curves treated from Fig. 7.
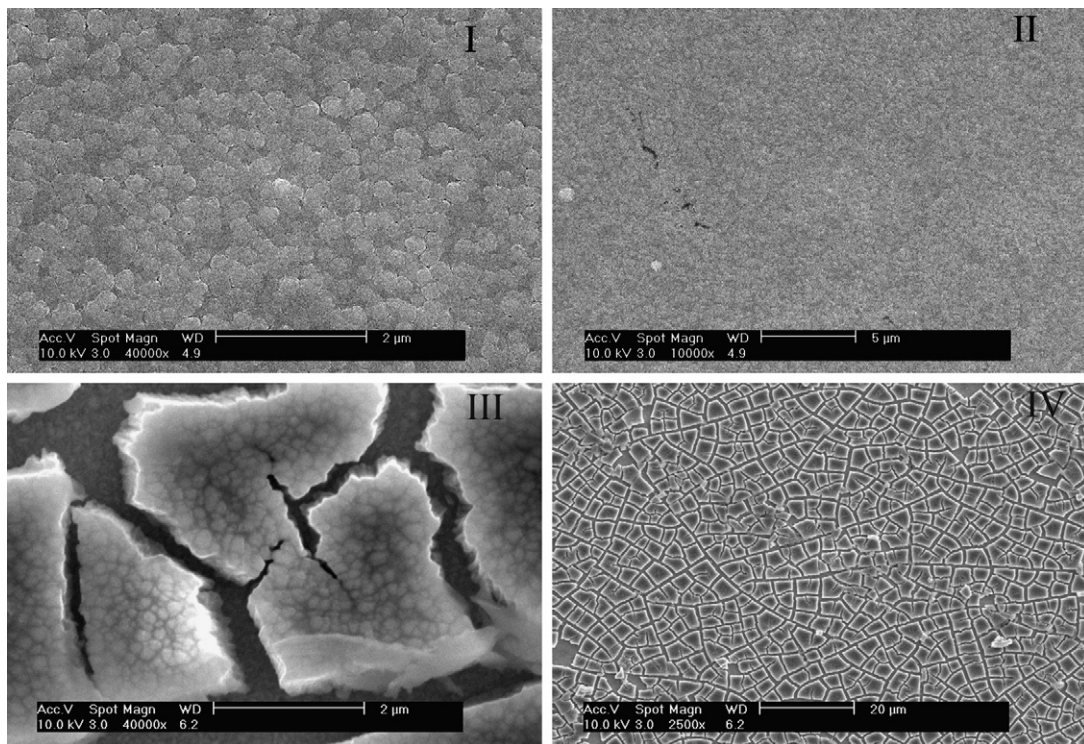

Fig. 10. SEM top-view images of the thin film electrode *a*: (I, II) initial film; (III, IV) after the 10th charge.

2) The three Ti–Si nanocomposite thin films show finer cracks after 10 cycles than the pure silicon thin film. The Ti–Si thin film *a* in which the grain size of the Ti$_x$Si$_y$ alloy is larger and the film is thicker shows much larger cracks than that of the films *b* and *c*.

3) It seems that the cracks tend to propagate along the grain boundaries.

A detailed statistical analysis regarding the fractured particle size, crack width and junction angles are shown in
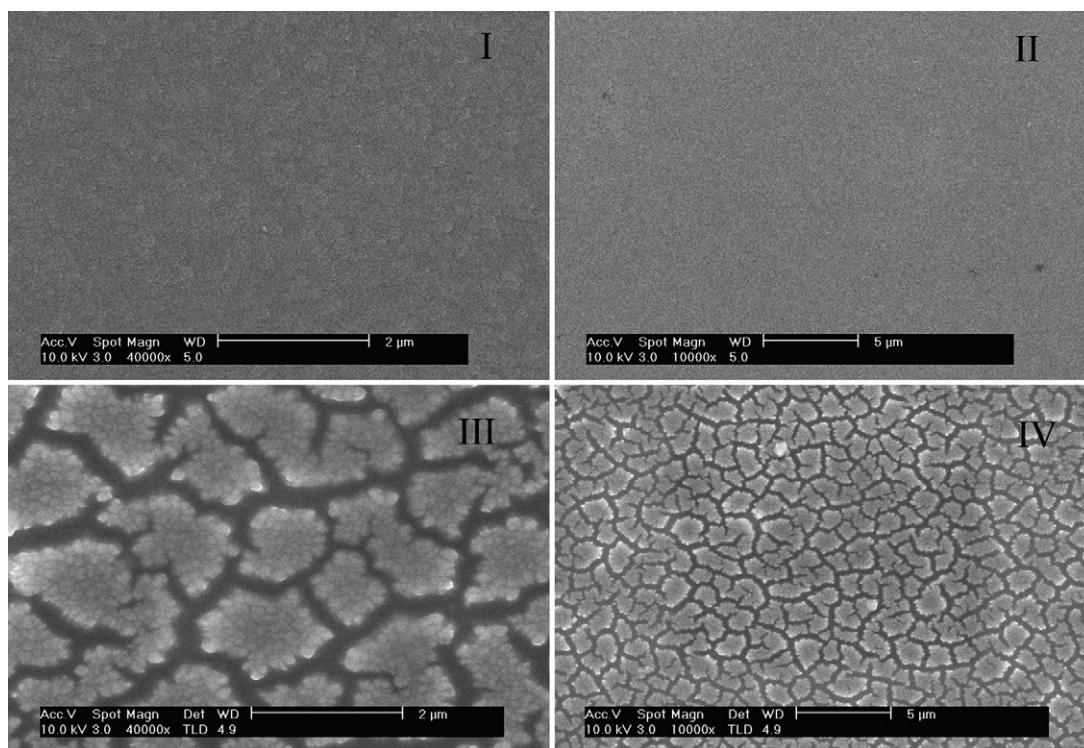
Fig. 11. SEM top-view images of the thin film electrode *b*: (I, II) initial film; (III, IV) after the 10th charge.

Figs. 14, 15 and 16 respectively. In Fig. 14, it is seen that the size of the fractured particles is smallest in the film *c*, with the largest area being less than $4\,\mu m^2$. The width of the cracks is less than $0.5\,\mu m$ in the films *b* and *c*, as shown in Fig. 15. The film *d* shows the widest cracks although the film thickness of the film *d* is thinner than the film *a*.

It is also interesting to note that the junction angles of most fractured particles in all cycled electrodes are 90°, as shown in Fig. 16. Similar patterns have been observed in a 500 nm amorphous Si thin film after 5 cycles [29]. A similar angle distribution has been also reported in the crack patterns of a Fe_2O_3 nanocrystal film under isotropic and unilateral stresses [30]. The angle of each corner in
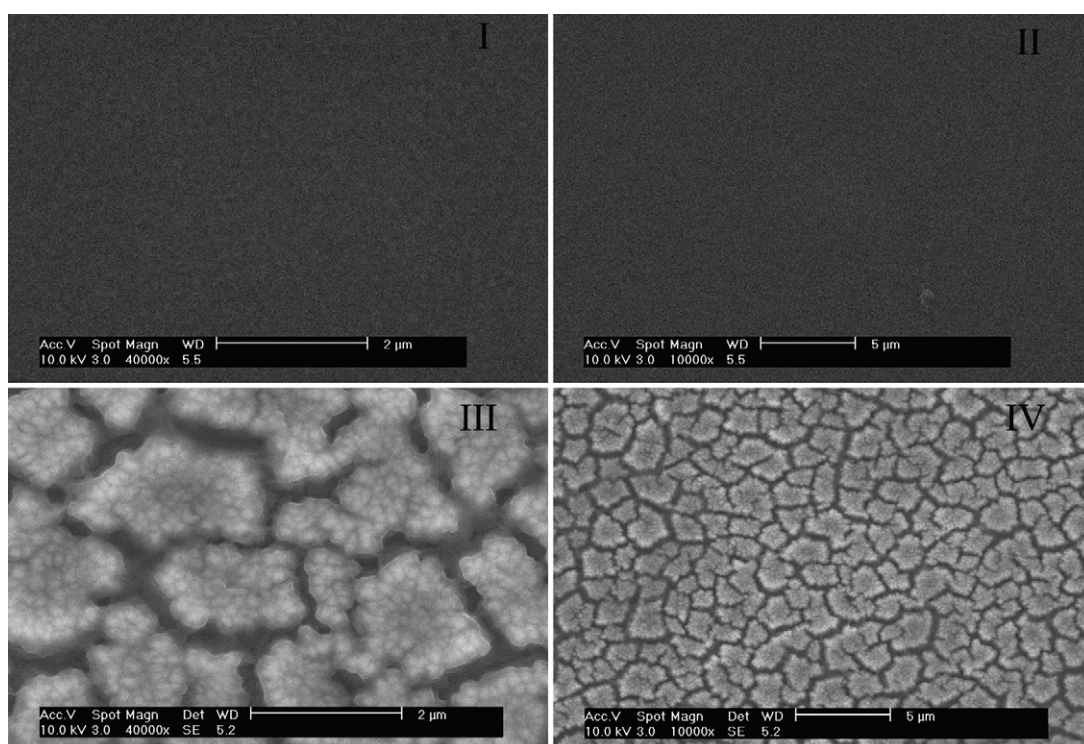

Fig. 12. SEM top-view images of the thin film electrode *c*: (I, II) initial film; (III, IV) after the 10th charge.
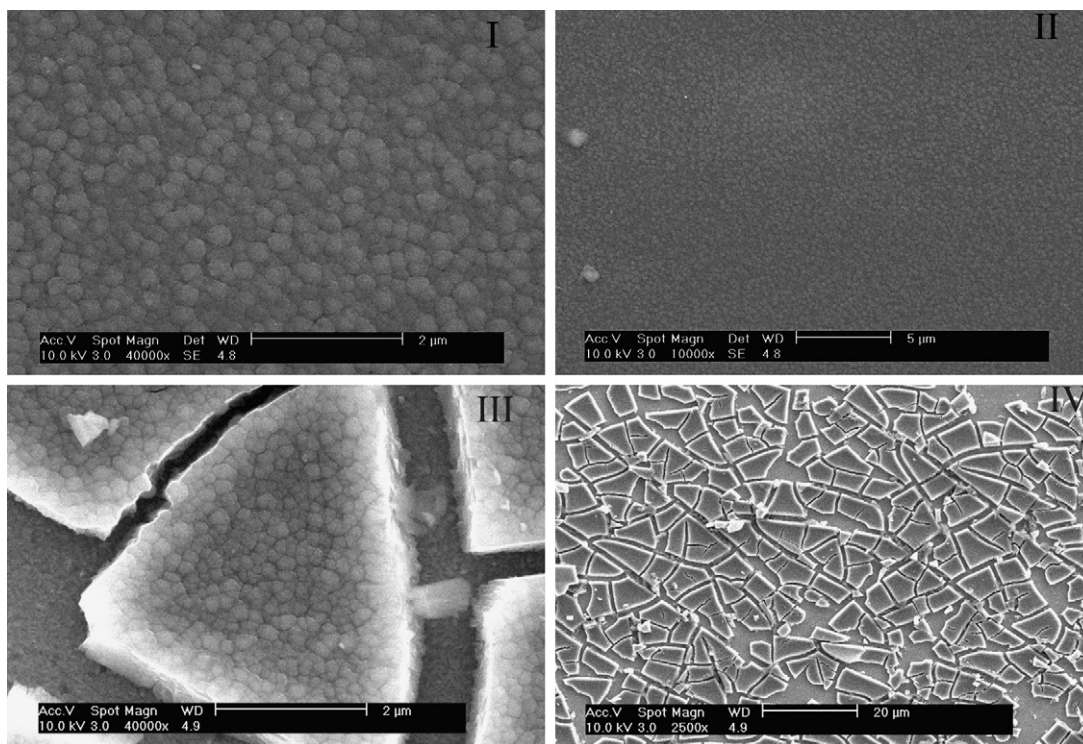
Fig. 13. SEM top-view images of the thin film electrode *d*: (I, II) initial film; (III, IV) after the 10th charge.

the remained fractured particles in all films is counted in Fig. 16. It is found that the angle distribution in the films *a*–*d* is a rough Gaussian distribution, centered at 90°. Film *d* shows the narrowest distribution, while the films *b* and *c* show a wider distribution.

Although similar fracture patterns have been documented in Si thin film anodes and the crack issues caused by lithiation and delithiation have been discussed recently [29,31–35], no analysis exists similar to that of Figs. 14–16.

It is of interest, therefore, to go a step further, and try to relate the present experimental results with theoretical predictions. A recent theoretical model has been developed which illustrates that thin film anodes are more prone to fracture than other lower surface area configurations [34], however, an analytical expression predicting the particle size after fracture has not been applied, thus far. In [36] it was shown that upon fracture of a metallic thin film

on a metal substrate the ultimate tensile strength (S) of the film is given by

$$S = \frac{2\bar{\lambda}_o^{sat}\tau_f}{3h}, \tag{1}$$

which implies that

$$\bar{\lambda}_o^{sat} = \frac{3Sh}{2\tau_f} \tag{2}$$

where h is the film thickness, S is the ultimate tensile strength of the film, τ_f is the ultimate shear strength between the film interface and the substrate, and λ_o^{sat} is the shortest distance between cracks in 1-dimension. Hence, λ_o^{sat}, can provide an estimate for the smallest fractured particle size observed upon fracture of the thin film anodes at hand. This size, however, can be obtained directly
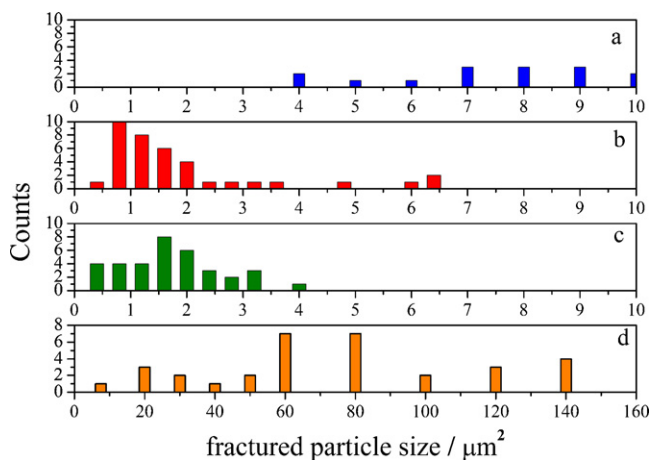

Fig. 14. Accounts of the fractured particle size of the four thin film electrodes *a*–*d* after the 10th charge shown in Figs. 10–13.
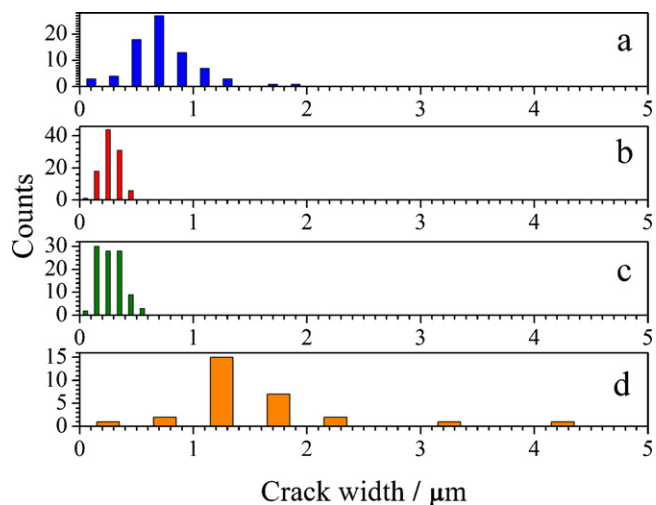

Fig. 15. Accounts of the crack width of the four thin film electrodes *a*–*d* after the 10th charge shown in Figs. 10–13.

Table 3
Comparing prediction of Eq. (2) for smallest fractured particle size, with experimental value from Fig. 14.

Films	Thickness, nm (h)	Ultimate tensile strength (S)	Ultimate interface shear strength, MPa (τ_f)	Smallest fractured particle size predicted from Eq. (2) ($\bar{\lambda}_o^{sat}$)	Smallest fractured particle observed from Fig. 14
a	480	400 MPa	80	3.6 μm	2 μm
b	250	215 MPa	100	0.8 μm	0.71 μm
c	250	215 MPa	100	0.8 μm	0.71 μm
d	250	2 GPa	100	7.5 μm	2.8 μm

from Fig. 14 for films a, b, c and d as 4 μm^2, 0.5 μm^2, 0.5 μm^2 and 7.5 μm^2, respectively.

In order to test Eq. (2) against the experimental data, the ultimate tensile strength (S) for the amorphous Si and TiSi$_2$ thin films and the ultimate shear strength between the film and Ti substrate (τ_f) must be known. In [37] it was shown that τ_f can be approximated by the yield stress of the substrate; hence for all thin film anodes $\tau_f \sim 100$ MPa, since this is the yield strength for Ti, which was the substrate. The ultimate tensile strength for amorphous Si could not be found in the literature, hence, that of polycrystalline Si thin films, $S = 2$ GPa [38], will be used for the film d. Similarly, the tensile strength for TiSi$_2$ thin films could not be found, and hence the value for single crystal TiSi$_2$, $S = 215$ MPa [39], will be used for films b & c. In [40] it was shown that the tensile strength in thin films increases as their thickness increases, hence for the thicker film a, it is assumed that $S = 400$ MPa. Inserting these values in Eq. (2), along with the film thickness provided in Table 1, it is estimated that the smallest fractured particle is $\bar{\lambda}_o^{sat} = 3.6$μm, 0.8 μm, 0.8 μm and 7.5 μm, for the films a, b, c and d respectively. This rough approximation is in very good agreement with the data of Fig. 14, particularly, for film b and c they are in precise agreement. A detailed comparison between Eq. (2) and the experimental data is provided in Table 3.

This is the first study to show that continuum mechanics predictions regarding fracture are in quantitative agreement with experimental data from fractured anodes, even though the diffusion of the Li-ions, and resulting expansion, was not explicitly accounted for in the mechanics framework. Previous theoretical mechanics studies [31,32,34] provided only a qualitative comparison with experimental data. This encourages the development of new theoretical frameworks for a more detailed understanding of fracture during lithiation.

It is of interest that both theory and experiment show more damage (larger fracture particles) for film d; this was anticipated by its poor electrochemical response. In order to increase the capacity retention, the Si mechanical stability must be increased, and this is achieved by the addition of Ti. In this connection it can be noted that more detailed mechanical studies have indeed shown that, in general, the existence of disilicide (VSi$_2$, CrSi$_2$) toughens the silicon alloy [41]. The observed crack resistance mechanism of the obtained Ti–Si nanocomposite thin films therefore is related to crack bridging and crack deflection, but needs to be further clarified in future studies.

The above results indicate clearly that dispersing tiny Ti$_x$Si$_y$ alloy grains in the amorphous Si film is another effective way to suppress the formation of large cracks, besides decreasing the film thickness. Since the existence of Ti$_x$Si$_y$ alloy grains have no significant influence on the thermodynamic or kinetic properties of the amorphous Si thin film, it is shown that the improvement in the mechanical properties is a key factor to improve the cyclic performance.

4. Summary

Compared to an amorphous pure silicon thin film, it is clear that the Ti–Si nanocomposite thin films with smaller Ti$_x$Si$_y$ alloy grain dispersed within an amorphous silicon matrix results in better cyclic performance. The electrochemical performance is directly related to fracture, since the Si thin film which showed the poorest capacity retention, exhibited the larger directional cracks and larger fractured particles, after 10 cycles, while the Ti–Si films were characterized by finer and wiggled cracks and a smaller fractured particle size. The junction angle in all thin films is distributed around 90° in a Gaussian distribution. A theoretical model was applied to predict the smallest size of the fractured particles in all thin films, and it was found to be in good agreement with the experimental measurements. This is the first step towards performing a more detailed study relating the mechanical stability and electrochemical performance of Si-based thin films. Both experiment and theory were consistent in predicting a smallest particle size of (~0.71–2.8 μm) for the Si-based thin film anodes examined. Based on these initial results a thin film will not continuously fracture upon Li-insertion, but once a critical size of the fractured particles is reached, further fragmentation will stop. This suggests that a more optimum microstructure for Si-based thin films would be patterned Si or Si pillars. The diameter of these structures would have to be below the smallest fracture particle size observed in the present study in order to result in minimal fracture. Such configurations are currently being studied.
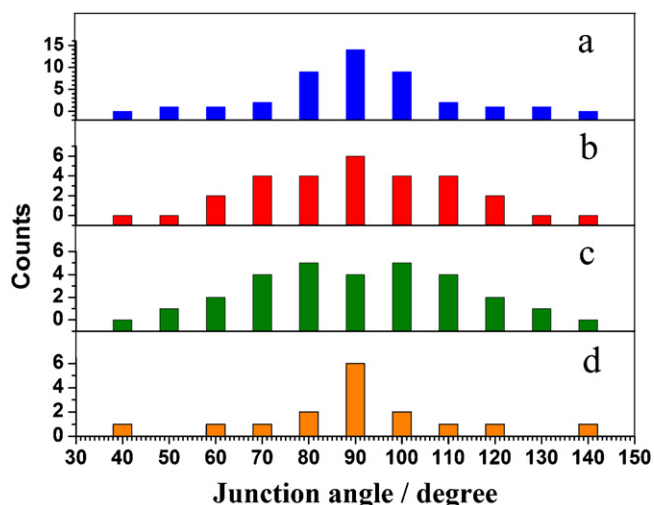
Fig. 16. Accounts of the junction angle distribution of the fractured particles of the four thin film electrodes a–d after the 10th charge shown in Figs. 10–13.

References

[1] R.A. Sharma, R.N. Seefurth, J. Electrochem. Soc. 123 (1976) 1763.
[2] B.A. Boukamp, G.C. Lesh, R.A. Huggins, J. Electrochem. Soc. 128 (1980) 725.
[3] R.A. Huggins, J. Power Sources 81 (1999) 13.
[4] H. Li, X.J. Huang, L.Q. Chen, Z.G. Wu, Y. Liang, Electrochem. Solid State Lett. 2 (1999) 547.
[5] H. Li, X.J. Huang, L.Q. Chen, G.W. Zhou, Z. Zhang, D.P. Yu, Y.J. Mo, Solid State Ionics 135 (2000) 181.
[6] G.W. Zhou, H. Li, H.P. Sun, D.P. Yu, Y.Q. Wang, X.J. Huang, L.Q. Chen, Z. Zhang, Appl. Phys. Lett. 75 (1999) 2447.
[7] R.L. Turner, D.J. Mcclure, L.J. Krause, M.M. Buckett, J.R. Dahn, O. Mao, US 6 203 944, 2001.
[8] S. Kawakami, M. Asao, US 6 949 312, 2005.
[9] S. Mizutani, H. Inoue, US Pat. Appl. 0208378, 2005.
[10] S. Mizutani, Y. Kudo, US Pat. Appl. 0121348, 2006.
[11] A.D.W. Todd, R.E. Mar, J.R. Dahn, J. Electrochem. Soc. 154 (2007) A597.
[12] K.T. Lee, Y.S. Jung, S.M. Oh, J. Am. Chem. Soc. 125 (2003) 5652.
[13] W.M. Zhang, J.S. Hu, Y.G. Guo, S.F. Zheng, L.S. Zhong, W.G. Song, L.J. Wan, Adv. Mater. 20 (2008) 1160.
[14] J. Yang, Y. Takeda, N. Imanishi, C. Capiglia, J.Y. Xie, O. Yamamoto, Solid State Ionics 152–153 (2002) 125–129.
[15] G.X. Wang, L. Sun, D.H. Bradhurst, S. Zhong, S.X. Dou, H.K. Liu, J. Power Sources 88 (2000) 278.
[16] A. Netz, R.A. Huggins, W. Weppner, J. Power Sources 119–121 (2003) 95.
[17] J.W. Kim, J.H. Ryu, K.T. Lee, S.M. Oh, J. Power Sources 147 (2005) 227.
[18] H. Ikeda, M. Fujimoto, S. Fujitani, Y. Doumoto, H. Yagi, H. Tarui, N. Tamura, R. Ohshita, M. Kamino, I. Yonezu, Proceedings of the Presentation at the 42nd Battery Symposium in Japan, Yokohama, Japan, November 21–23, 2001.
[19] K. Sayama, H. Yagi, Y. Kato, S. Matsuta, H. Tarui, S. Fujitani, Proceedings of the Presentation at the IMLB 11, Montreal, CA, USA, June 23–28, 2002, 2002.
[20] T. Takamura, S. Ohara, M. Uehara, J. Suzuki, K. Sekine, J. Power Sources 129 (2004) 96.
[21] Y.L. Kim, H.Y. Lee, S.W. Jang, S.H. Lim, S.J. Lee, H.K. Baik, Y.S. Yoon, S.M. Lee, Electrochimica Acta 48 (2003) 2593.
[22] S.J. Lee, H. Young Lee, Y.S.##H. Park, K. Baik, S.M. Lee, J. Power Sources 119–121 (2003) 117.
[23] J.B. Kim, H. Young Lee, K.S. Lee, S.H. Lim, S.M. Lee, Electrochem. Commun. 5 (2003) 544.
[24] S.J. Lee, H. Young Lee, H.K. Baik, S.M. Lee, J. Power Sources (2003) 119–121.
[25] B.S. Jeon, S.M. Lee, Electronic Mater. Lett. 5 (2009) 13–17.
[26] W.Y. Yang, H. Iwakuro, H. Yagi, T. Kuroda, S. Nakamura, Jpn. J. Appl. Phys. 23 (1984) 1560.
[27] A.A. Galuska, J.C. Uht, N.J. Marquez, Vac. Sci. Technol. A 6 (1988) 110.
[28] K. Kawade, A. Suzuki, K. Tanaka, J. Phys. Soc. Jpn. 69 (2000) 777.
[29] J.C. Li, A.K. Dozier, Y.C. Li, F.Q. Yang, Y.T. Cheung, J. Electrochem. Soc. 158 (2011) A689.
[30] J. Richardi, A.T. Ngo, M.P. Pileni, J. Phys. Chem. C 114 (2010) 17324.
[31] K.E. Aifantis, J.P. Dempsey, J. Power Sources 143 (2005) 203–211.
[32] K.E. Aifantis, S.A. Hackney, J.P. Dempsey, J. Power Sources 165 (2007) 874–879.
[33] X. Xiao, P. Liu, M.W. Verbrugge, H. Haftbaradaran, H. Gao, J. Power Sources 196 (2011) 1409.
[34] K.E. Aifantis, S.A. Hackney, J. Power Sources 196 (2011) 2122.
[35] F.Q. Yang, J. Power Sources 196 (2011) 465.
[36] D.H. Timm, B.B. Guzina, V.R. Voller, Int. J. Solid Struct. 40 (2003) 125.
[37] B.F. Chen, J.F. Hwang, G.P. Yu, J.H. Huang, Surf. Coat. Technol. 126 (2000) 91.
[38] T. Tsuchiya, O. Tabata, J. Sakata, Y. Taga, J. Microelectromech. Syst. 7 (1998) 106.
[39] S. Takeuchi, T. Hashimoto, Intermetallics 2 (1994) 289.
[40] T. Tadashi, A. Hirozumi, S. Noda, Jpn. J. Appl. Phys. 33 (1994) 171.
[41] D.S. Fischer, Thesis for Doctor of Philosophy in Materials Science and Engineering at the Massachusetts Institute of Technology, September, 2010.